Radiative Examination of Developing African Easterly Waves and Saharan Dust Interactions: Comparative Insights from Reanalysis and NASA Airborne Observations

Ruby W. Burgess [1] and Mayra I. Oyola-Merced [1]

[1]University of Wisconsin-Madison, Madison, WI 53706, USA

Correspondence: Ruby W. Burgess (rwburgess@wisc.edu)

Abstract. This study thoroughly examines the impact of aerosols on atmospheric heating rates over the North Atlantic Ocean, with a specific focus on developing African Easterly Waves (AEWs). It utilizes data from the NASA DC-8 aircraft, dropsonde profiles, lidar observations, and satellite-based precipitation data obtained during NASA's CPEX-CV field campaign, as well as MERRA-2 and CAMS reanalyses. Using a four-stream radiative transfer model, the research focuses specifically on days

5   characterized by Saharan dust coinciding with AEWs and tropical storm development and also contrasts its findings with a notable dust-only event in June 2020. The findings reveal notable differences in shortwave (SW) and longwave/infrared (LW/IR) heating rates, underscoring the persistent challenges in accurately representing aerosol effects in the atmosphere, even after assimilating observational data. These discrepancies persisted on days with both background and high dust concentrations, emphasizing the challenges in accurately representing aerosol radiative effects in models and highlighting the urgent need for

10   improved aerosol representation in reanalysis datasets.

1 Introduction

Over the past two decades, substantial advancements have been made in characterizing aerosol properties, as well as in identifying their spatiotemporal distribution and their influence on the planet's radiative equilibrium (Ramanathan et al., 2001). This research has culminated in the recognition that aerosols have both a "direct effect" on climate by altering the Earth's radia-

15   tive budget and redistributing heat throughout the atmosphere, as well as an "indirect effect" by impacting cloud formation, precipitation, and optical properties (IPCC, 2023). These effects are contingent on the concentration and altitude of aerosols (Lyapustin et al., 2011; Bauer and Menon, 2012; Xu et al., 2017). In the same period, significant strides have been made in aerosol modeling, data assimilation techniques for Numerical Weather Predictions (NWP) applications, and the development of precise 3-D aerosol models. These developments have enabled a more accurate representation of aerosols in weather mod-

20   els and reanalysis, leading to improvements in forecast accuracy (Mulcahy et al., 2014; Toll et al., 2016). Furthermore, these advancements have opened new avenues for advanced research on aerosol effects and provided the potential for monitoring air quality events. Nevertheless, uncertainties persist, especially concerning the atmosphere's response to various physical properties of aerosols, particularly on daily timescales that affect weather patterns (Mulcahy et al., 2014; Toll et al., 2016; Zhang

et al., 2016). This is due to significant limitations in accurately characterizing aerosols, which are crucial for forecasting and

25 understanding the evolution of weather systems and processes.

Aerosols, with characteristics such as concentration, size distribution, composition, vertical distribution, hygroscopicity, and mixing state, dynamically influence heating rates in the Earth's atmosphere. This influence stems from their complex interplay, orchestrating radiative processes within large-scale weather systems. For example, aerosol concentration significantly dictates the scattering and absorption of solar radiation, leading to regional variations in heating rates. Similarly, size distribution

30 of aerosol particles governs their efficacy in scattering or absorbing radiation, impacting temperature gradients and atmospheric stability. Composition is pivotal, inducing localized atmospheric heating or cooling. Vertical distribution intricately shapes aerosol radiative effects across distinct atmospheric levels. Hygroscopic properties alter aerosol optical characteristics as they interact with water vapor, and mixing state complicates their radiative consequences. Therefore, understanding these aerosol-induced changes in heating rates is crucial for enhancing the accuracy of weather forecasting models and the reliability

35 of reanalysis data. This knowledge enables a more precise representation of atmospheric processes and the development of weather systems.

The North Atlantic basin provides the setting for these processes to coexist. On a protagonist role are the African Easterly Waves (AEWs, Burpee, 1972; Reed et al., 1988; Thorncroft and Blackburn, 1999). Along with the African Easterly Jet (AEJ), they are the primary triggers of regional and synoptic weather events over the Atlantic basin (Reed et al., 1977), having devas-

40 tating societal consequences over Africa, the Caribbean and the United States. Studies show, for example, that the AEJ-AEW system influences convection and rainfall over West Africa (Carlson, 1969; Reed et al., 1977), while more than half of the tropical cyclones that have been observed to develop over the eastern Atlantic Ocean have AEW origins (Landsea et al., 1998). Another important phenomenon is the Saharan dust (and associated Saharan Air Layer, SAL), a prominent aerosol feature that covers a vast portion of the Atlantic Ocean during boreal Spring and Summer (Carlson and Prospero, 1972; Dunion and

45 Velden, 2004). The Saharan dust is believed to alter both short wave (SW) and longwave/infrared (LW/IR) solar radiation (Dunion and Velden, 2004) as well as temperatures at the surface and aloft (Nalli and Stowe, 2002; Oyola, 2015), decrease vertical wind shear, induce thermodynamic stability, and most notably, influence the genesis of tropical storms and hurricanes (Dunion and Velden, 2004; Pratt and Evans, 2009). Given that they share similarities in seasonality and geographical extent, the AEWs and Saharan dust are consequently coupled to influence each other. The United States Geostationary Operational

50 Environmental Satellites (GOES) satellite imagery on Fig. 1 depicts an example of these interactions. On larger timescales, processes like the AEW trigger Saharan dust lofting by enhancing diurnal emission mechanisms (Dunion and Velden, 2004). On the other hand, dust atmospheric feedbacks influence the AEWs through direct and indirect radiative effects (Grogan and Thorncroft, 2019). We have advanced our understanding on how Saharan dust affects AEW's structure and evolution, however, despite more than two decades of studies, no conclusive evidence has been agreed upon. From the observational/reanalysis

55 standpoint, most studies examining the effects of Saharan dust on AEWs analytical approaches have produced contradictory results, and/or have only focused on attributing AEW growth or decay to dust-induced changes in the static stability alone (e.g. Karyampudi et al., 1999; Jones et al., 2004; Reale et al., 2009; Jury and Santiago, 2010; Reale et al., 2011; Ma et al., 2012). A significant limitation with these studies, and a possible reason behind their discrepancies, is that most focus on to-
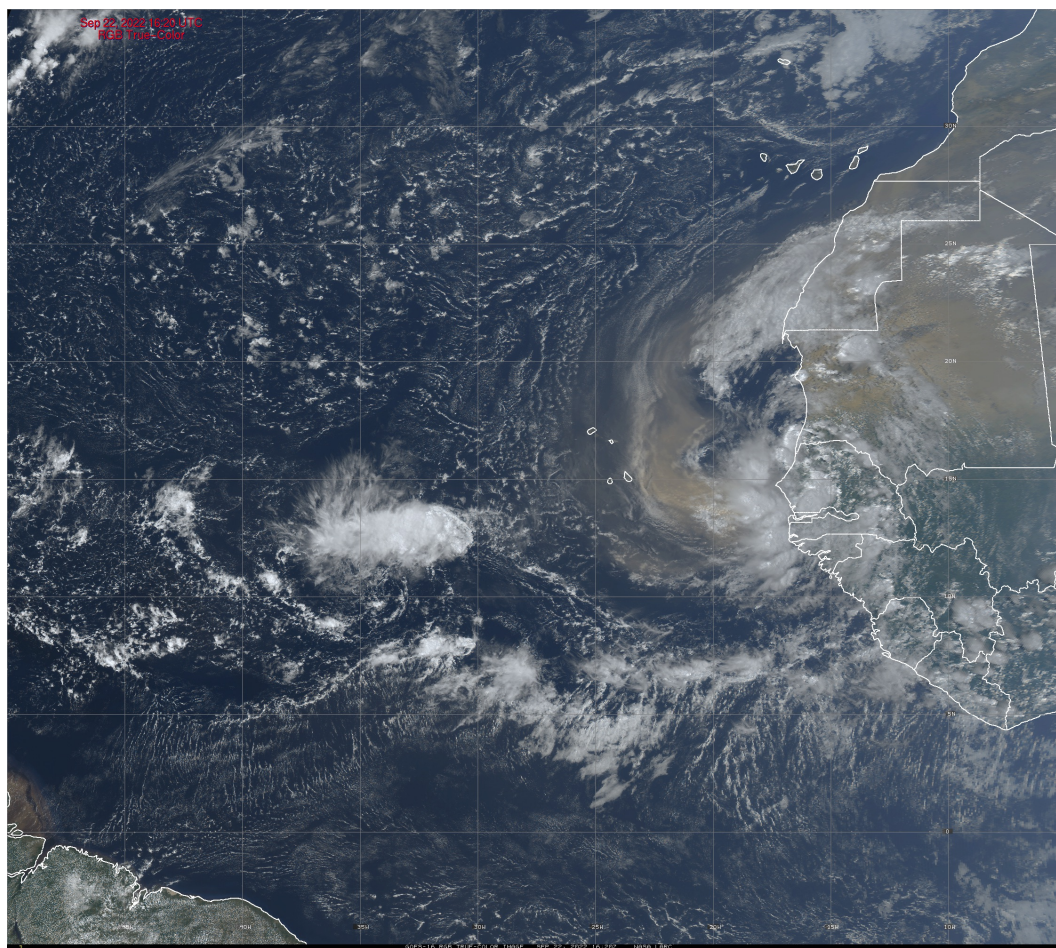
Figure 1. GOES-16 image of dust interacting with an African Easterly Wave on 22 September 2022 during the CPEX-CV field campaign (GOES-R Series Program, 2019).

tal column aerosol loading (or AOD) but have failed to properly address the relationship between the AEWs and changes in the vertical distribution of dust aerosols. Also, these studies do not directly address the dust impact at different stages of the AEW, nor clearly discretize changes in airmass in both systems with transatlantic passage. Although it seems a straightforward issue to address, previous research has been limited because retrieving good-quality measurements of vertical profiles of atmospheric parameters (moisture, wind, temperature, and vertical information of aerosols) in Saharan dust events remains an extremely challenging endeavor, particularly in the lower atmosphere, as most of these techniques are biased due to changes in atmospheric composition itself (Nalli et al., 2011; Oyola, 2015).

There is an opportunity to characterize the impact of dust aerosols in AEWs, aiming to enhance our comprehension of their feedback mechanisms. This can be achieved by leveraging radiative transfer, aerosol vertical data from reanalysis, and, when accessible, utilizing existing field campaign datasets for atmospheric closure experiments. Obtaining high-resolution

3

aerosol profiles from observations poses a significant challenge, particularly over oceanic regions, however, when such data is accessible, it can contribute significantly to addressing some of the questions that remain unanswered.

In this study, we integrate data collected during the airborne National Aeronautics and Space Administration (NASA) Convective Processes Experiment – Cabo Verde (CPEX-CV) and profiles from two different global reanalyses into a four-stream radiative transfer model. Our primary objective is to perform a radiative examination of the interactions between AEWs and Saharan Dust during the intensive observation period (IOP). The CPEX-CV datasets provide a distinctive opportunity for this model evaluation, featuring collocated aircraft instrumentation that simultaneously measured high-resolution vertical aerosol profiles with dropsondes over AEWs. Utilizing this in situ instrumentation, our goal is to assess the reanalyses' accuracy in depicting aerosol radiative properties. Specifically, within the observational constraints of the limited dataset available for this study, our objectives include understanding the magnitude of aerosol heating rates—particularly those associated with dust—and considering their potential influence on AEW development and model representation.

2 Data and methods

The analysis was conducted over the North Atlantic Ocean, in a box spanning 0°to 25°N and 15°W to 35°W to the west of the Sahara Desert. Data from several reanalyses and the CPEX-CV field campaign were used to analyze the effects of aerosols on atmospheric profiles and their impact on the development of AEWs.

2.1 CPEX-CV

CPEX-CV was conducted between 1 and 30 September 2022 out of Cabo Verde over the North Atlantic. Its objectives included examining the interplay of atmospheric dynamics, properties of the marine boundary layer, convection, the Saharan Air Layer and Saharan dust, and their interactions at different spatial scales. The mission aimed to enhance our comprehension and predictive capabilities regarding the lifecycles of processes such as AEWs, aiming to increase our understanding of such processes in a data-scarce region such as the tropical East Atlantic. During the field campaign, data were collected during fourteen research flights from the NASA DC-8 aircraft by several instruments including the ones described below. We make use of data from the seven research flights that coincided with a developing AEW.

2.1.1 AVAPS dropsondes

The Advanced Vertical Atmospheric Profiling System or AVAPS (Hock, 1999), is a dropsonde system providing vertical profiles of pressure, temperature, specific humidity, and winds that was used onboard the DC-8 during CPEX-CV. Dropsondes were launched at multiple locations during each flight. The profile altitude was limited to the DC-8 aircraft's maximum altitude of 42,000 ft, and most profiles did not contain data above 200 hPa. We employ 64 dropsonde profiles of pressure, temperature, and specific humidity throughout seven research flights to characterize atmospheric conditions in our analysis.

2.1.2 HALO

The NASA Langley High Altitude Lidar Observatory or HALO (Bedka et al., 2021) is a lidar system operated from an air-
borne platform to provide nadir-viewing profiles of water vapor, methane columns, and profiles of aerosol and cloud optical
properties. The HALO profiled the vertical distribution of aerosol in the atmosphere during each of the research flights used
in our analysis. We utilize the 532 nm aerosol extinction coefficient as a measure of extinction coefficient. We use mean daily
profiles of pressure, temperature, and specific humidity from HALO to calculate mean heating rates for two days of interest
(09 and 22 September). The latitude and longitude data from this dataset were used to determine the flight track location for
each flight used in the analysis.

2.2 MERRA-2

The Modern-Era Retrospective Analysis for Research and Applications, Version 2 (MERRA-2, Buchard et al., 2017; Gelaro
et al., 2017; Randles et al., 2017) is a reanalysis dataset developed by NASA that provides comprehensive and high-quality
atmospheric data from 1980 onward, including the assimilation of aerosols and a representation of their interactions with other
physical processes. We utilize the 3D 6-hourly Analyzed Meteorological Fields dataset (or inst6_3d_ana_Nv on 72 levels)
for profiles of pressure, temperature, specific humidity, and ozone mixing ratio. For aerosol, we utilize the inst3_3d_aer_Nv
collection, which includes instantaneous 3-dimensional 3-hourly data within MERRA-2. This dataset encompasses assimilated
aerosol mixing ratio parameters at 72 model layers, including dust, sulfur dioxide, sea salt, black carbon, and organic carbon.
Similarly, we also obtain 3-hourly Aerosol Optical Depth (AOD) Analysis from the inst3_2d_gas_Nx.

An additional treatment is required to be able to obtain extinction profiles from dust concentration. We calculate extinction
coefficient from each dust mixing ratio profile bin concentration profile at each level from dust mixing ratio for each of the five
bins provided in the aerosol mixing ratio dataset, using the following equation:

$$\beta_e = k_e \rho_{air} = \frac{3R_{DU}Q_{ext}}{4r\rho_p}\rho_{air} \tag{1}$$

where k_e is the mass extinction coefficient in m^2 kg^{-1}, ρ_{air} is the air density in kg m^{-3}, R_{DU} is the dust mass mixing ratio
for a specific bin in kg kg^{-1}, Q_{ext} is the extinction efficiency, r is the particle radius in m, and ρ_p is the particle density in kg
m^{-3}. The air density was provided by the MERRA-2 analyzed meteorological fields. The particle radius used for each of the
five bins is 0.73 μm, 1.4 μm, 2.4 μm, 4.5 μm, 8.0 μm respectively. The particle density is 2500 kg m^{-3} for particles of mean
radius of 0.73 μm, and 2650 kg m^{-3} for the rest of the bins (GMAO, 2023). The extinction efficiency was approximated for
each bin using values from GMAO (2023) that correspond to the closest particle radius for each bin. The data collected during
the CPEX-CV campaign were assimilated into the MERRA-2 reanalysis, and our analysis examines the performance of the
assimilation.

2.3 CAMS

It is noteworthy to mention that the CPEX-CV data were assimilated into the MERRA-2 reanalysis dataset used in this study. We use the Copernicus Atmosphere Monitoring Service reanalysis (CAMS, Inness et al., 2019), which did not assimilate data

130 from CPEX-CV, as a reference to assess the impacts of assimilation on the reanalysis. CAMS is a reanalysis dataset that comprises 3D time-consistent atmospheric composition fields, including aerosols, chemical species, and greenhouse gases. We utilize the 3-hourly datasets on 25 pressure levels for temperature, specific humidity, and dust aerosol mixing ratio at three different particle size ranges (0.03 - 0.55 μm, 0.55 - 0.9 μm, 0.9 - 20 μm), as well as the total column AOD at 550 nm. Similar to the MERRA-2 dataset, we calculate the extinction coefficient at each level for the 3 dust bins listed above using the following

135 formula:

$$\beta_e = k_e \rho_{air} = \frac{3R_{DU}Q_{ext}}{4r\rho_p} \cdot \frac{p}{R_d T_v} \tag{2}$$

where $T_v = (1 + 0.61q)T$ and p is the pressure in hPa, R_d is the gas constant for dry air in J kg^{-1} K^{-1}, T_v is the virtual temperature in K, q is the specific humidity in kg kg^{-1}, and T is the temperature in K. The pressure, specific humidity, and temperature were provided by the CAMS dataset. Since CAMS also uses GOCART aerosol properties, the values for extinction

140 efficiency, particle radius, and particle density for each of the three bins are the same used for MERRA-2 for particle radii sizes of 0.24 μm, 0.8 μm, and 8 μm respectively. Similar to the MERRA-2 dataset, the values for extinction were added together to calculate the total dust aerosol extinction. Because each bin represents a range of particle sizes and the extinction efficiency depends on particle size, the accuracy of the extinction coefficient remains limited for both the MERRA-2 and CAMS datasets.

2.4 IMERG

145 The Integrated Multi-satellitE Retrievals for Global Precipitation Measurement (IMERG, Huffman et al., 2020) is a dataset developed and provided by NASA that offers global precipitation data by merging and integrating data from the Global Precipitation Measurement (GPM) satellite constellation. We leverage the daily mean data within the IMERG dataset to identify and track the sampled AEWs within our designated geographic region. To delve deeper into the dust-AEW intricate interplay, we superimpose IMERG data with the MERRA-2 total dust mixing ratio dataset as in Fig. 2. This integrated approach allows

150 us to explore how and where dust aerosols may be influencing AEW dynamics, providing a more comprehensive view of the factors affecting AEW behavior.

2.5 Data processing

2.5.1 Observational analysis

The MERRA-2 total dust concentration was derived by aggregating the contributions from five distinct dust mixing ratio bins.

155 To explore the dynamics of dust in relation to convection and precipitation, we superimposed MERRA-2 total dust mixing ratio onto IMERG daily accumulated precipitation, enabling the creation of daily maps (e.g. Fig. 2). These maps provided valuable insights into the interplay between dust and AEWs. In the process of our analysis, we leveraged these maps, in conjunction
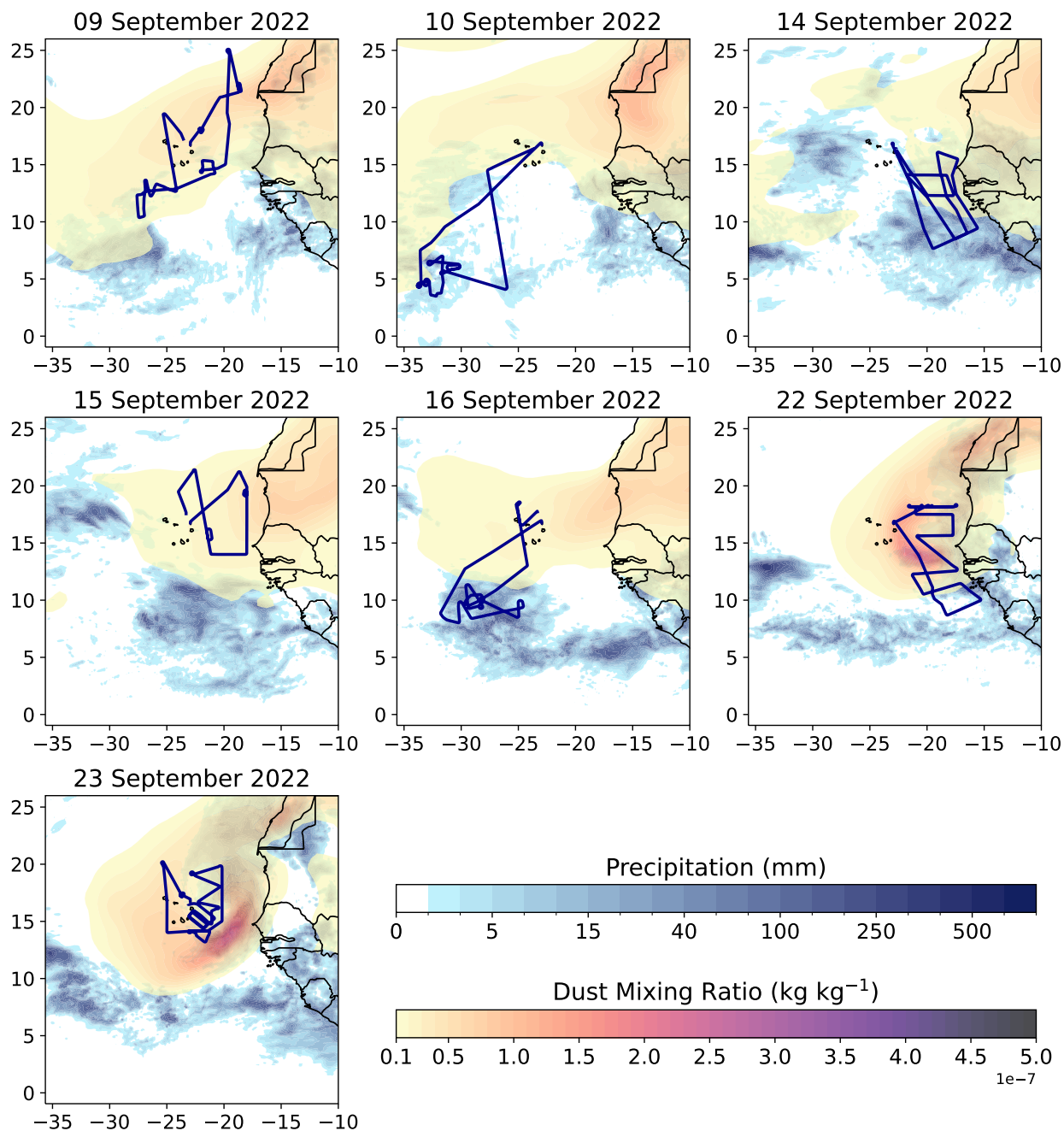
Figure 2. Flight tracks (blue) with overlaid total dust mixing ratio from MERRA-2 and daily accumulated precipitation from IMERG for seven of the research flights during the CPEX-CV field campaign.

with the daily forecast reports from CPEX-CV to identify specific days of interest. Furthermore, we utilized these maps to track the temporal evolution of dust concentration throughout the field campaign. Additionally, we assessed the integration of
160 CPEX-CV data into the MERRA-2 reanalysis, examining how this assimilation impacted the overall dataset.

2.5.2 Data processing for radiative transfer

We use the positional data from the CPEX-CV HALO dataset to collocate data from the two reanalyses (MERRA-2 and CAMS) with the CPEX-CV dataset. We process the AVAPS dropsonde data to select profiles of pressure, temperature, and specific humidity with sufficient information to be run in the Fu-Liou-Gu radiative transfer model (Gu et al., 2011). We generate
165 profiles from MERRA-2 and CAMS reanalysis at the same location. Similarly, we process extinction profiles from HALO to select profiles providing sufficient aerosol extinction information. We select extinction profiles from the HALO, MERRA-2, and CAMS datasets matching the location of the selected dropsonde profiles, and interpolate these to 72 levels, restricting the profiles to below the 100 hPa level. We calculate a mean pressure, temperature, specific humidity and extinction profile from the HALO dataset for each flight as well as corresponding profiles from both reanalyses. These profiles, which are interpolated
170 to 72 levels, are used to analyze daily mean heating rates on 09 September and 22 September. Values of AOD were retrieved for each location using the 532 nm Total Optical Thickness from CPEX-CV, Aerosol Optical Depth Analysis from MERRA-2 and Total Aerosol Optical Depth at 550 nm from CAMS.

2.6 Fu-Liou-Gu Radiative Transfer Model (FLG RTM)

The Fu-Liou-Gu (FLG) radiative transfer (RT) model is used to calculate heating rates and irradiances (fluxes) from the dif-
175 ferent datasets described above. The FLG RT scheme, as proposed by Gu et al. (2011), represents an upgraded iteration of FLG originally developed by Fu and Liou in 1992 and 1993. This refined model offers improved parameterizations for aerosol properties, which enable more accurate simulation of radiative effects, aligning more closely to real-world observations. The delta-four-stream approximation is utilized for solar radiative flux calculations (Liou et al., 1988) and the delta-two-and-four-stream approximation is employed for LW/IR radiative flux calculations (Fu et al., 1997) in the model. The model divides the
180 solar and LW/IR spectra into 6 and 12 bands respectively, determined by the locations of absorption bands, and the calculations incorporate the of absorption by the H2O continuum and various minor absorbers within the solar spectrum in addition to the principal absorbing gases.

2.6.1 OPAC

The current FLG radiation scheme contains a total of 18 aerosol types parametrized by the Optical Properties of Aerosols and
185 Clouds (OPAC, Hess et al., 1998) database. This database provides humidity-aware single-scattering properties for spherical aerosols computed from Lorenz Mie theory, for 60 wavelengths in the spectral region between 0.3 μm and 40 μm. These 60 bands are interpolated into the 18 bands of the FLG RT scheme. The 18 types of aerosol include maritime, continental, urban, five size bins for mineral dust, insoluble, water soluble, soot (BC), sulfate droplets, sea salt in two modes (accumulation

and coarse mode), and mineral dust in four different modes (nucleation, accumulation, coarse, and transported mode). For the
190   purposes of this study, we employ the mineral dust transported mode.

2.6.2 Calculation of heating rates

Following a similar approach to (Oyola et al., 2019), we run the model ingesting atmospheric profiles from the three datasets
(MERRA-2, CAMS, and CPEX-CV) to retrieve heating rates throughout the vertical layer at each of the selected dropsonde
locations. Simulations are performed after taking the solar zenith angle at the corresponding local time and location into
195   consideration. The heating rates are given by (e.g. Petty, 2008):

$$
\mathcal{H}(z) \equiv -\frac{1}{\rho(z)C_p} \Bigg\{ -[F_i^{\uparrow}(0) - \Delta\tilde{v}_l \pi \bar{B}_l(z)]\frac{\partial\tau_i(0,z)}{\partial z}
$$
$$
- [F_i^{\downarrow}(\infty) - \Delta\tilde{v}_l \pi \bar{B}_l(z)]\frac{\partial\tau_i(z,\infty)}{\partial z}
$$
$$
- \Delta\tilde{v}_l \pi \int_z^{\infty} [\bar{B}_l(z') - \bar{B}_l(z)]\frac{\partial^2\tau_i(z,z')}{\partial z'dz}dz'
$$
$$
- \Delta\tilde{v}_l \pi \int_0^z [\bar{B}_l(z') - \bar{B}_l(z)]\frac{\partial^2\tau_i(z',z)}{\partial z'dz}dz' \Bigg\} \tag{3}
$$

where $\rho(z)$ is the air density at level z, C_p= 1005 J kg^{-1} K^{-1} is the specific heat capacity of air at constant pressure, τ_i is
the band average flux transmittance, $\tilde{v}_l$ represents the spectral interval or band (SW, LW/IR), $F_i^{\uparrow}, F_i^{\downarrow}, F_i^{\uparrow}(0), F_i^{\downarrow}(\infty)$ are fluxes
where the arrows represent the direction of incoming flow (from surface up from top of atmosphere to surface), and the indices
200   0 and ∞ represent the surface and TOA respectively. In its summarized form, the heating rate equation can be stated as:

$$
\mathcal{H}(z) \equiv -\frac{1}{\rho(z)C_p}\frac{\partial F_{net}}{\partial z} \tag{4}
$$

Here, F_{net} is the net flux given by the difference between upward and downward directed fluxes. We set a control run for each
profile where no aerosol feedback is included and a parallel run using the extinction profiles calculated from each of the three
respective datasets, for each of the profile locations.

205   ### 2.6.3 Categorization of background and anomalous AOD cases

We define a threshold of AOD < 0.2 calculated from the CPEX-CV 532 nm total optical thickness to select background dust
concentration profiles. We obtain 32 dropsonde locations which fit the condition of background AOD (AOD < 0.2), and we
select profiles from all three datasets at these locations. We then select the top 32 dropsonde locations with highest AOD
calculated from CPEX-CV 532 nm total optical thickness and define these as anomalous dust concentration profiles, and select
210   profiles from all three datasets at these locations. The resulting mean AOD value for the background and anomalous cases for
each dataset are shown in Table 1. The profiles selected for the background and anomalous cases for MERRA-2 and CAMS
are based on the CPEX-CV AOD threshold, not MERRA-2 and CAMS AOD values, and thus have a differing range of AOD

Table 1. Mean AOD for background and anomalous cases over the seven research flights for CPEX-CV, MERRA-2 and CAMS.

Dataset	Mean Background AOD	Mean Anomalous AOD
CPEX-CV	0.09	0.83
MERRA-2	0.22	0.46
CAMS	0.27	0.33

values. The 64 dropsonde profiles of temperature, specific humidity, and extinction are ingested into the FLG RTM, which is run for all three datasets (CPEX-CV, MERRA-2, and CAMS) at each dropsonde location at the time of launch. We refer to these runs as the aerosol-aware case. A control run where the aerosol parameter was turned off was also performed for each run. The mean shortwave (SW), longwave/infrared (LW/IR), and total heating rate differences between the aerosol runs and the control runs are calculated using the FLG RTM. The results are plotted for background dust concentration profiles in Fig. 4 and for anomalous dust concentration profiles in Fig. 5.

3 Results and discussion

3.1 Description of AEW events during CPEX-CV

In our analysis, we focused on data collected within a region defined by latitudes ranging from $0°$ to $25°$ N and longitudes from $15°$ to $35°$ W. During the CPEX-CV field campaign, the fourteen DC-8 research flights sampled 10 different African Easterly Waves (AEWs) identified as AEW 1 through AEW 10. Four of these waves developed into named tropical storms (AEW 4, 5, 6, 8), with two intensifying into hurricanes (AEW 4, 6). For this study, we utilized profiles collocated with dropsondes obtained during developing AEW events, which correspond to the flights on 9, 10, 14, 15, 16, 22, and 23 September, resulting in 64 profiles over 4 AEWs or their surrounding environments. Table 1 provides specific information about these developing AEWs. Environmental conditions varied for each flight, as illustrated in Fig. 2, which displays flight tracks for several days of interest and corresponding weather conditions. Integrated dust concentration from MERRA-2 and accumulated IR-MW precipitation from IMERG highlight different regimes sampled, such as conditions where mainly dust is present (09 and 15 September), conditions where the "dusty" outer environment relative to the AEW was sampled (14 September), and situations where AEWs interacted with heavy dust loadings (22-23 September).

On 09 September, AEW 4 was located off the west coast of Africa, later evolving into Tropical Storm Fiona on 14 September and further intensifying into a hurricane on 18 September. Fiona reached Category 4 with the highest 1-minute sustained winds of 140 mph (220 km/h) and produced catastrophic damage to many islands in the Caribbean. On 23 September, it transitioned into an Extratropical Cyclone, directly impacting the Atlantic portion of Canada and becoming the costliest cyclone in Canadian history. It finally dissipated on 27 September 2022. The DC-8 aircraft sampled the early stages of this storm on 09 September (first panel, Fig. 2), and the resulting data are analyzed in our study.

Table 2. Flight date, time, location, mean and maximum AOD, location relative to AEW and corresponding tropical cyclone for seven days corresponding to a developing AEW.

Flight Date	Flight times	Location	Mean AOD	Max AOD	Location Relative to AEW	Corresponding TC
09 September	12:06:35 to 20:40:03 UTC	$10.4° - 25.1°$N, $18.5°$W $- 27.6°$W	0.25	1.69	In AEW 4 region	Fiona
10 September	13:42:27 to 21:19:37 UTC	$3.5° - 16.9°$N, $22.9°$W $- 33.8°$W	0.07	0.26	In AEW 4 region	Fiona
14 September	09:03:44 to 16:27:09 UTC	$7.7° - 16.9°$N, $15.6°$W $- 23.0°$W	0.06	1.02	Between AEW 5 and AEW 6	Gaston and Ian
15 September	15:04:47 to 20:26:22 UTC	$14.0° - 21.4°$N, $18.0°$W $- 24.0°$W	0.36	1.10	North of AEW 6	Ian
16 September	12:52:20 to 20:26:15 UTC	$8.0° - 18.6°$N, $22.9°$W $- 31.8°$W	0.23	1.14	In AEW 6 region	Ian
22 September	04:53:21 to 12:36:42 UTC	$8.7° - 18.4°$N, $15.3°$W $- 23.0°$W	1.02	3.34	In AEW 8 region	Hermine
23 September	06:48:29 to 14:17:34 UTC	$13.2° - 20.2°$N, $20.2°$W $- 25.5°$W	0.52	1.51	In AEW 8 region	Hermine

AEW 5 moved off the west coast of Africa on 12 September, initially producing disorganized showers and thunderstorms, but eventually developing into Tropical Storm Gaston on 20 September. Gaston dissipated by 25 September when additional
240   strengthening was prevented by colder and drier air intrusion. Between 14 and 15 September, AEW 6 moved off the west coast, transforming into Tropical Storm Ian on 24 September and intensifying into a hurricane on 26 September. The research flight on 14 September flew between AEW 5 (TS Gaston, second Panel Fig. 2) and AEW 6 (Hurricane Ian, second Panel Fig. 2), while the flight on 15 September traversed north of AEW 6, sampling a dust storm located in the outer storm environment of the AEW (third Panel Fig. 2).

245   On 22 September, AEW 8 moved off the African coast, transforming into Tropical Storm Hermine on 23 September before weakening back to a tropical depression on 24 September. This storm, coinciding with the highest concentrations of Saharan dust sampled during the CPEX-CV field campaign, was studied on 22nd and 23rd September, and the resulting data are included in our analysis (fourth and fifth panel, Fig. 2). Additional detailed information on developing AEWs is provided in Table 2.

250   3.2   Impact of aerosol on heating rates

Profiles of mean temperature in Kelvin (top row), specific humidity in kg/kg (middle row), and aerosol extinction in km^{-1} (bottom row) which were utilized in the radiative transfer calculation are depicted in Fig. 3. The grey shading shows the spread of all profiles used in the RTM. CPEX-CV data (considered as the truth) is shown in the left column, while the other two columns show the collocated mean profiles and corresponding spread obtained from MERRA-2 and CAMS reanalysis. The
255   temperature and moisture profiles across the three datasets exhibit striking similarities. The specific humidity profiles exhibit high variability in all three datasets (CPEX-CV, MERRA-2, and CAMS), reflected in larger spread for all three datasets. This points to a broader and more diverse distribution of specific humidity values, particularly noticeable in the region between the surface and 800 hPa.

On the other hand, comparisons reveal significant disparities when examining aerosol extinction profiles. At this point, it
260   is noteworthy to remind the reader that MERRA-2 assimilated data collected during CPEX-CV. Despite the assimilation of CPEX-CV data into MERRA-2, MERRA extinction profiles exhibit much higher surface extinction compared to the CPEX-CV data (particularly in the atmospheric layer between 1000 – 900 hPa), however, missing most of the variability throughout the tropospheric column that the HALO profiles were able to capture, including several notable aerosol layers around 800, 700, and 650 hPa. In the case of MERRA-2, most of the aerosol is confined to the first 600 hPa. The contrast becomes
265   even more pronounced when comparing the CPEX-CV and MERRA-2 against CAMS extinction. CAMS underestimates the extinction by an order of magnitude in several portions of the troposphere. Interestingly enough, the differences found for aerosol loading are not only confined to the extinction profiles, but there are also noticeable differences in AOD. The mean AOD for background and anomalous cases over the seven research flights for CPEX-CV, MERRA-2, and CAMS are summarized in Table 1. There are significant differences in the mean observed AODs and the ones provided by the reanalysis. It seems the
270   reanalysis overestimates the AOD compared to the observations for background cases and underestimates for the anomalous cases. These differences will result in significant discrepancies in the heating rate calculations, as we will discuss below.
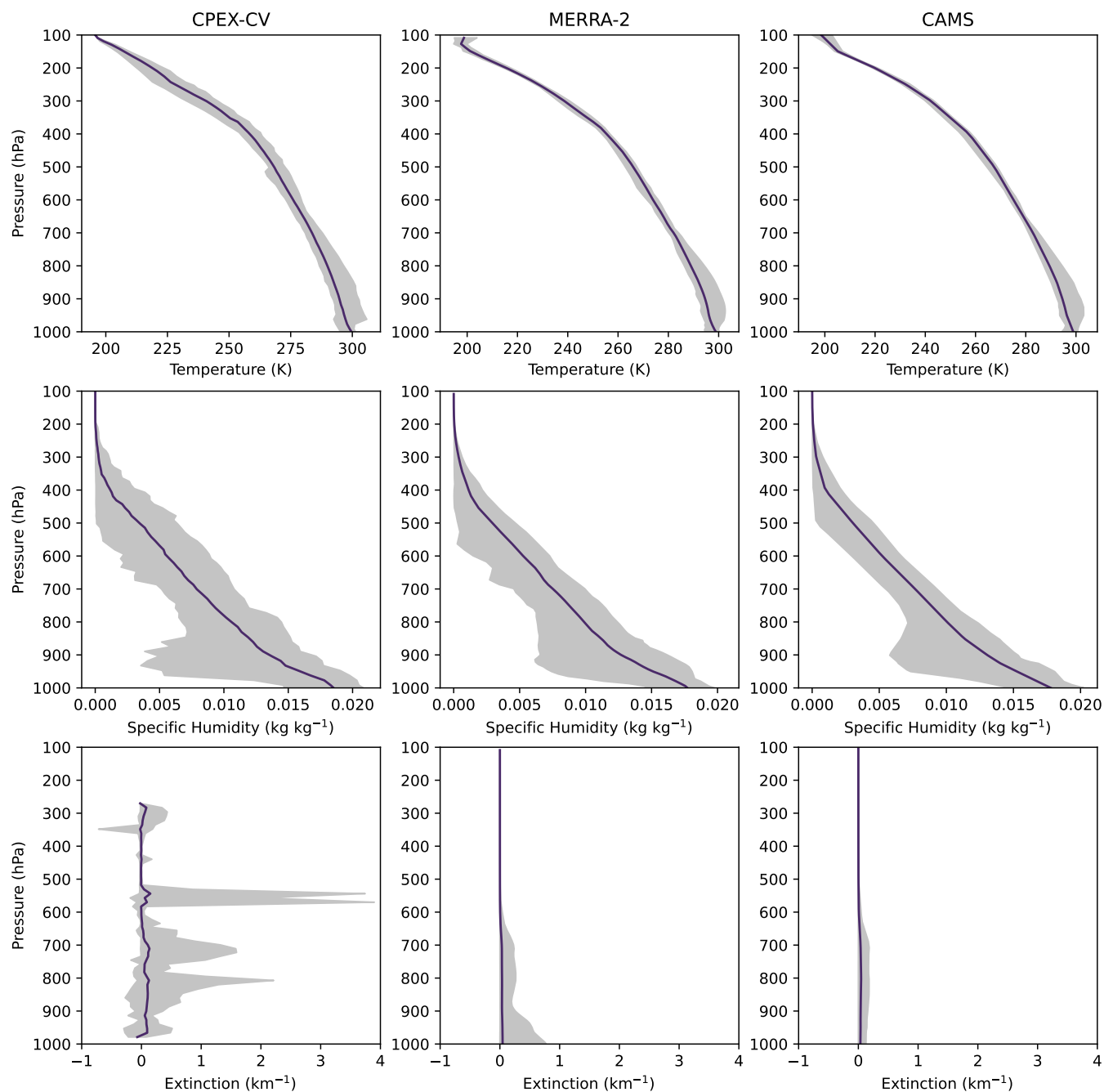
Figure 3. Temperature, specific humidity and extinction mean (magenta) and range (grey shading) for CPEX-CV, MERRA-2 and CAMS.

As mentioned before, 64 different cases were identified, all within a developing AEW or its environment. Each one of these cases use 3 datasets (CPEX-CV, MERRA-2, and CAMS), and for each of them, two RTM runs are performed: one without the
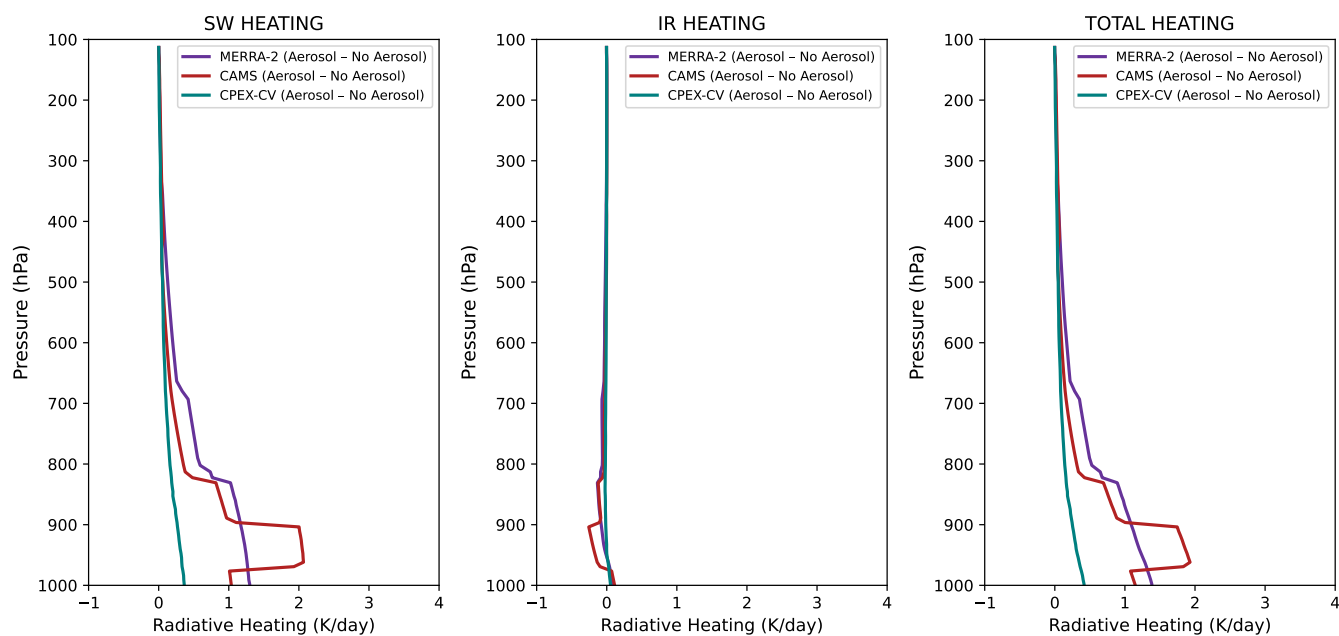
Figure 4. Heating rate difference between aerosol-aware and control run for MERRA-2 (purple), CAMS (red) and CPEX-CV (teal) for the background dust case. The left panel shows SW heating, the center panel shows LW/IR heating and the right panel shows total heating.

aerosol effect (RTM only initialized with pressure, temperature, specific humidity, and ozone), which we refer to as the control
275 run, and another one with all of the same atmospheric information and also aerosol extinction and corresponding AOD, which
we refer to as the aerosol-aware run, for a total of 384 runs. Fluxes (in W/m^2) and heating rates (in K/day) are thus calculated
for each one of the 384 cases. To better understand the impact of different dust loading scenarios, we categorize the data into
two groups based on dust AOD as sampled during CPEX-CV. We thus defined as background all profiles with AOD $\leq$ 0.2 and
select an equal number of profiles (32 profiles) with the highest AOD which are defined as "anomalous" or high (lowest AOD
280 that meets this criteria is 0.335). This approach resulted in a 50-50 data split; in other words, 50% of the profiles are labeled as
anomalous or high dust, while the lower 50% was classified as low or background dust.

We then proceeded to subtract the aerosol-aware run from the control run for each case to its corresponding dataset to evaluate
the impacts of dust on heating rates. We calculated the mean and corresponding standard deviations for our aerosol-aware
minus control profiles. Figure 4 shows the mean heating rates differences (aerosol-aware minus control) for low or background
285 dust and Fig. 5 for anomalous dust concentrations. Heating rate differentials are provided in three panels: shortwave (SW),
longwave/infrared (LW/IR), and total heating rate differences between the aerosol-aware run and the control run.

Figure 4 reveals notable discrepancies in the calculated heating rates differences, particularly in the SW contribution. The
differences in SW heating rate profiles, especially the significant divergence below 800 hPa, can be attributed to variations in
distribution (as indicated by extinction profiles), specifically the differences in AOD detailed in Table 2. CAMS reports the

290 highest mean AOD for the background cases, and this is reflected in both the vertical distribution and magnitude of heating rates, particularly below 900 hPa. Both reanalysis profiles exhibit significantly higher heating rates near the surface, exceeding 1 K, while the CPEX-CV profiles maintain a more modest increase, not exceeding 0.4 K in the same region. Interestingly, most of the contribution to total heating rates comes from SW processes rather than IR. The fact that most CPEX-CV sampling occurred during the morning and close to solar noon may explain some of this behavior, but it is not the sole factor and could

295 also be attributed to the choice of optical properties within the FLG RTM. Saharan dust, often composed of mineral-rich particles, can both absorb and scatter incoming sunlight. Consequently, the presence of Saharan dust in the atmosphere leads to the absorption of a significant portion of SW radiation, resulting in localized heating effects we observed in the differential of heating rates. The marginal disparity observed between aerosol and no-aerosol runs in SW radiation can be attributed to the inherent characteristics of the optical properties for transported dust within FLG, particularly their relatively subdued impact

300 in the SW spectral region.

Unlike certain aerosols that highly influence LW/IR radiation, dust aerosols, including those from Saharan dust, tend to exhibit lower absorption efficiency in the LW/IR spectrum. Their contribution to LW/IR radiative forcing is further limited by a dominance of scattering effects in SW radiation, where dust aerosols are more influential. Additionally, the intricate interplay of various radiative forcing components, including water vapor and greenhouse gases, may overshadow the specific impact of

305 dust aerosols in the LW/IR region. The size, composition, and altitude of dust particles also play roles in determining their radiative properties.

Figure 5 is similar to Fig. 4 but focuses on heating rates calculated for anomalous profiles with AOD exceeding 0.335 as defined previously. The impact on heating rates is evident when compared with Fig. 4; higher AOD values correspond to higher heating rates. However, notable differences are observed in the reanalysis data, with significantly higher heating rates below

310 800 hPa and smaller rates (compared to calculations using observed data) between 800 and 400 hPa. Additionally, there is an increase in LW/IR cooling below 800 hPa, particularly in comparison with the findings in Fig. 4

The marginal disparity observed between aerosol and no-aerosol runs in the LW/IR radiation can be explained by the inherent characteristics of the optical properties for transported dust within the model. Dust aerosols have a relatively subdued impact in the LW/IR spectral region, meaning they are less effective at absorbing and re-emitting LW/IR radiation compared to other

315 aerosols that might be more influential in this spectrum.

3.3 Dataset comparison

The impact of assimilating CPEX-CV data into the MERRA-2 reanalysis was assessed by comparing it with CPEX-CV profiles considered as the truth. The differences between the reanalysis and truth were examined for both aerosol-aware runs and control runs, specifically focusing on background and anomalous dust concentrations. In Fig. 6, the differences for background AOD

320 (AOD < 0.2) are depicted, while Fig. 7 illustrates the differences for anomalous AOD. In both figures, the purple line represents the heating rate difference between MERRA-2 and CPEX-CV (MERRA-2 minus CPEX-CV), and the red line represents the heating rate difference between MERRA-2 and CAMS (MERRA-2 minus CAMS). The solid lines correspond to the aerosol-aware run, while the dotted lines represent the control run.
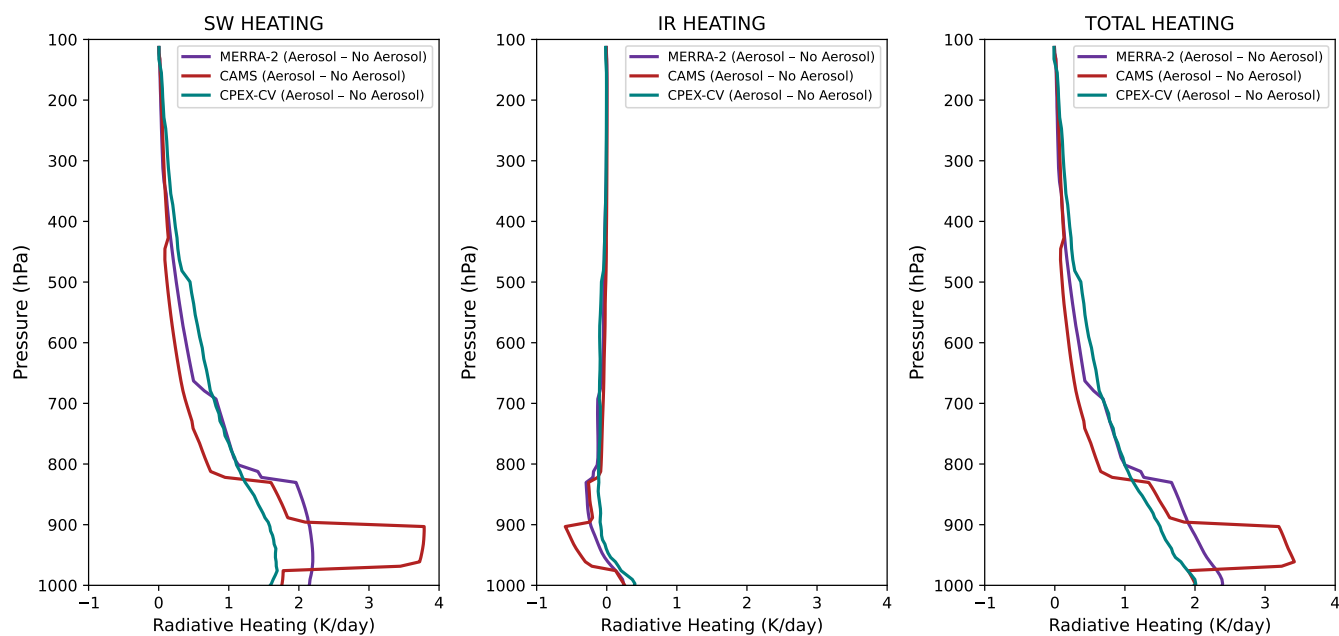
Figure 5. Heating rate difference between aerosol-aware and control run for MERRA-2 (purple), CAMS (red) and CPEX-CV (teal) for the anomalous dust case. The left panel shows SW heating, the center panel shows LW/IR heating and the right panel shows total heating.

Examining the background AOD case in Fig. 6, the difference in SW heating below 700 hPa is nearly 0 K/day for the
325 control case, increasing to around 0.7 K/day at the surface in the aerosol-aware run. For anomalous dust concentrations in Fig. 7, aerosol-aware runs exhibit similar differences in SW heating for MERRA-2 below 800 hPa. Regarding LW/IR heating, substantial differences between MERRA-2 and truth, reaching up to 1.7 K/day between 700 hPa and 500 hPa, are evident for both aerosol-aware and control runs. In the background dust case (Fig. 6), these differences in LW/IR heating are more pronounced, exceeding 2 K/day around 600 hPa. Smaller differences in LW/IR heating are observed for anomalous AOD
330 cases, reaching nearly 1.5 K/day around 700 hPa in Fig. 7. Importantly, these significant differences in heating rates persist at crucial atmospheric levels despite the assimilation of CPEX-CV data into MERRA-2.

For both background AOD and anomalous AOD cases, as shown in Fig. 6 and 7, the difference between CAMS and truth is almost 0 K/day for SW heating below 700 hPa in the control run. Notably, an increase of up to 1.5 K/day between 975 hPa and 900 hPa is observed in the aerosol-aware run for the background AOD case, and up to 2.2 K/day for anomalous dust cases. This
335 discrepancy suggests a potential misplacement of a dust layer by the reanalysis at this atmospheric level. Differences in LW/IR between CAMS and truth are evident between 700 hPa and 500 hPa for both aerosol-aware and control runs, reaching up to 0.8 K/day for both background AOD and anomalous AOD cases. Notably, these differences are smaller than those observed between MERRA-2 and truth, highlighting the persistent challenges even with MERRA-2's assimilation of CPEX-CV data.
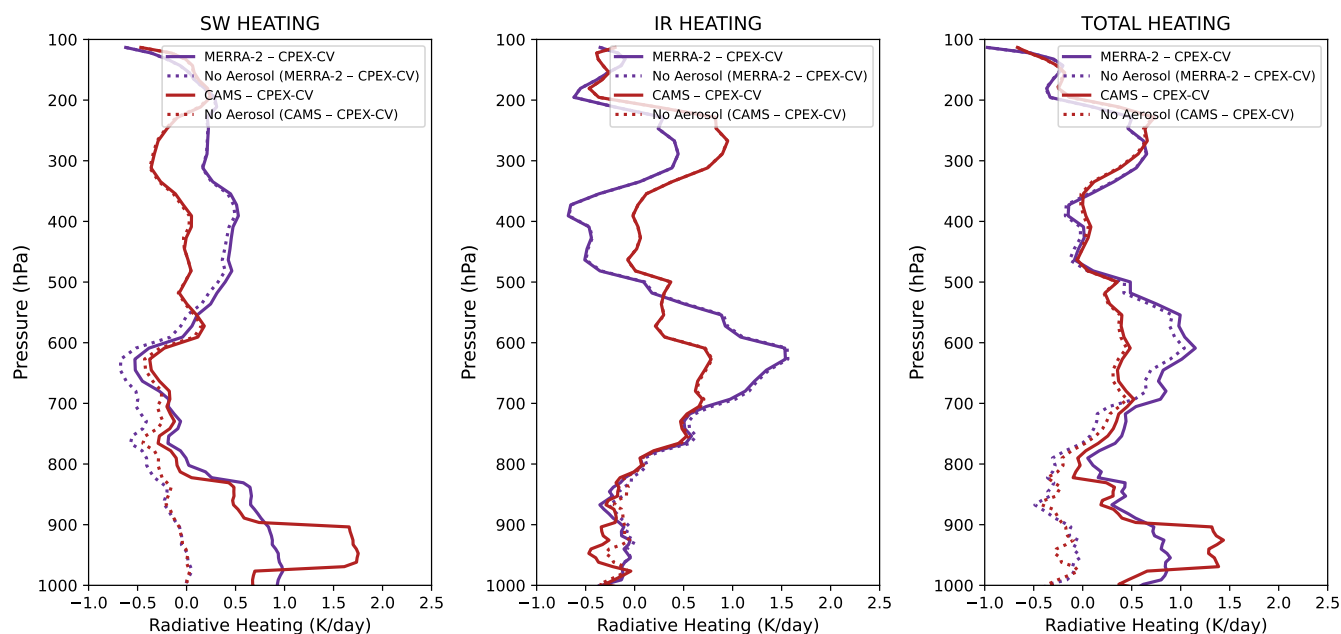
16

Figure 6. Heating rate difference between reanalysis and observation for the background dust case. Differences between MERRA-2 and CPEX-CV are plotted in purple and differences between CAMS and CPEX-CV are plotted in red. The solid lines correspond to the aerosol-aware run and the dotted lines correspond to the control run.

3.4 Comparison with an extreme dust event: The June 2020 Godzilla dust storm

340 To elucidate the distinctions in aerosol representation and subsequent impacts on heating rates between the MERRA-2 and CAMS reanalyses, specifically in the absence of cloud-related influences as encountered in the context of AEWs, we conducted a comparative analysis. This investigation focused on a notable event known as the Godzilla dust storm, an extreme dust-only occurrence in June 2020 within the same geographic region. Notably documented in the literature (Yu et al., 2021), the event showcased unprecedented AOD levels, as depicted in Fig. 8 for 18 June. The FLG RTM was employed to compute heating rates

345 for a profile situated at 15°N and 20°W at 12:00Z, corresponding to an AOD of 2.70. The resultant aerosol impact, as illustrated in Fig. 9, accentuates the increase in SW heating profiles. CAMS exhibits pronounced SW heating concentrated between 950 hPa and 900 hPa, while MERRA-2 displays lower peak values but a broader range extending from the surface to around 800 hPa. Interestingly, the LW/IR heating differences hover close to 0 K/day for both MERRA-2 and CAMS. These findings align consistently with our prior analysis conducted in September 2022, reinforcing the robustness of the observed profiles and the

350 utility of the FLG RTM in capturing the nuances of aerosol-induced heating variations outside of cloud-influenced scenarios associated with AEWs.
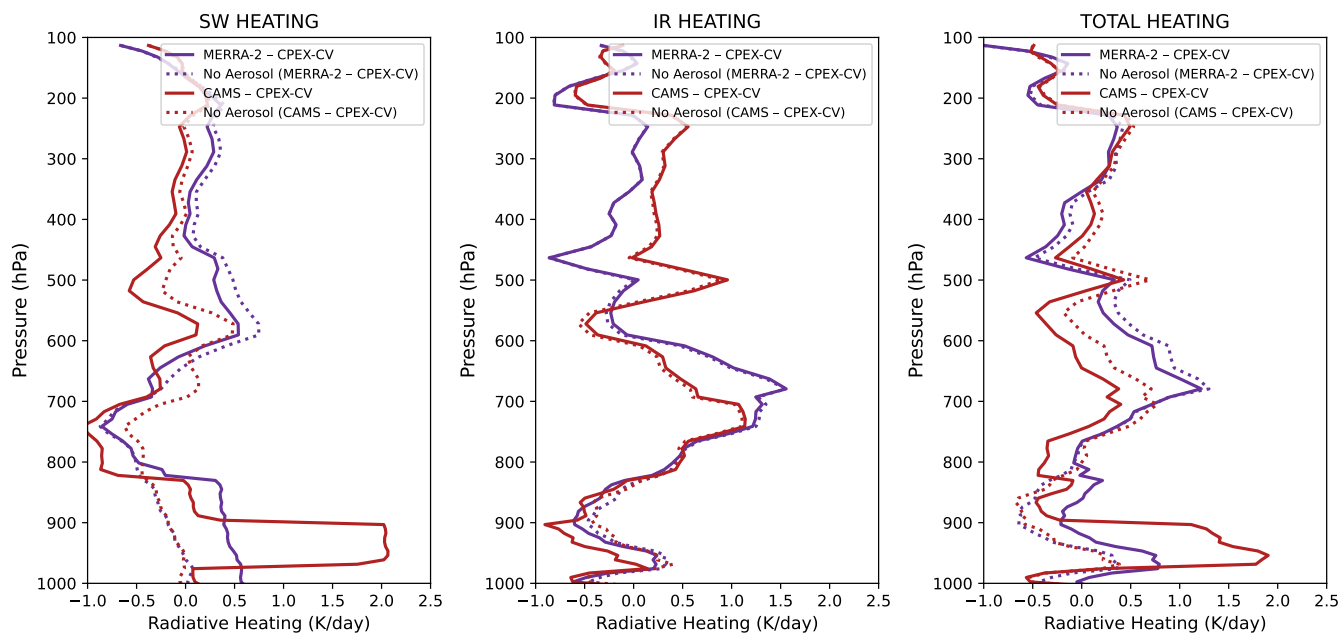
Figure 7. Heating rate difference between reanalysis and observation for the anomalous dust case. Differences between MERRA-2 and CPEX-CV are plotted in purple and differences between CAMS and CPEX-CV are plotted in red. The solid lines correspond to the aerosol-aware run and the dotted lines correspond to the control run.

3.5 Case study: Hurricane Fiona and TS Hermine

We analyze the effect of aerosol on heating rates for all three datasets on two days of interest (9 September 2022 and 22 September 2022), using mean profiles of pressure, temperature, specific humidity, and extinction from HALO averaged over the flight path. The RTM simulations are performed after taking into consideration the solar zenith angle at the mean local time and location of the flight. The research flight on 09 September flew through AEW 4, which later developed into Hurricane Fiona. The research flight on 22 September flew through AEW 8, which soon after developed into TS Hermine. Figure 10 illustrates the difference in aerosol mean heating rates between the aerosol-aware and control runs during the research flight on 09 September, where the average AOD value was 0.25 according to the CPEX-CV dataset. Figure 10 shows a SW heating of nearly 1 K/day at the surface which decreases with height for the CPEX-CV dataset. This SW heating rate is greatly overestimated by both the MERRA-2 and CAMS reanalyses, with a heating rate of 2 K/day at the surface for MERRA-2 and a heating rate of over 1.5 K/day at the surface for CAMS, reaching up to 3 K/day between 950 hPa and 900 hPa.

Figure 11 illustrates the difference in aerosol mean heating rates between the aerosol-aware and control run during the research flight on 22 September, where the average AOD value was 1.02. This shows a SW heating of nearly 2 K/day at the surface which stays around this value up to 700 hPa and then decreases with height for the CPEX-CV dataset. This SW heating
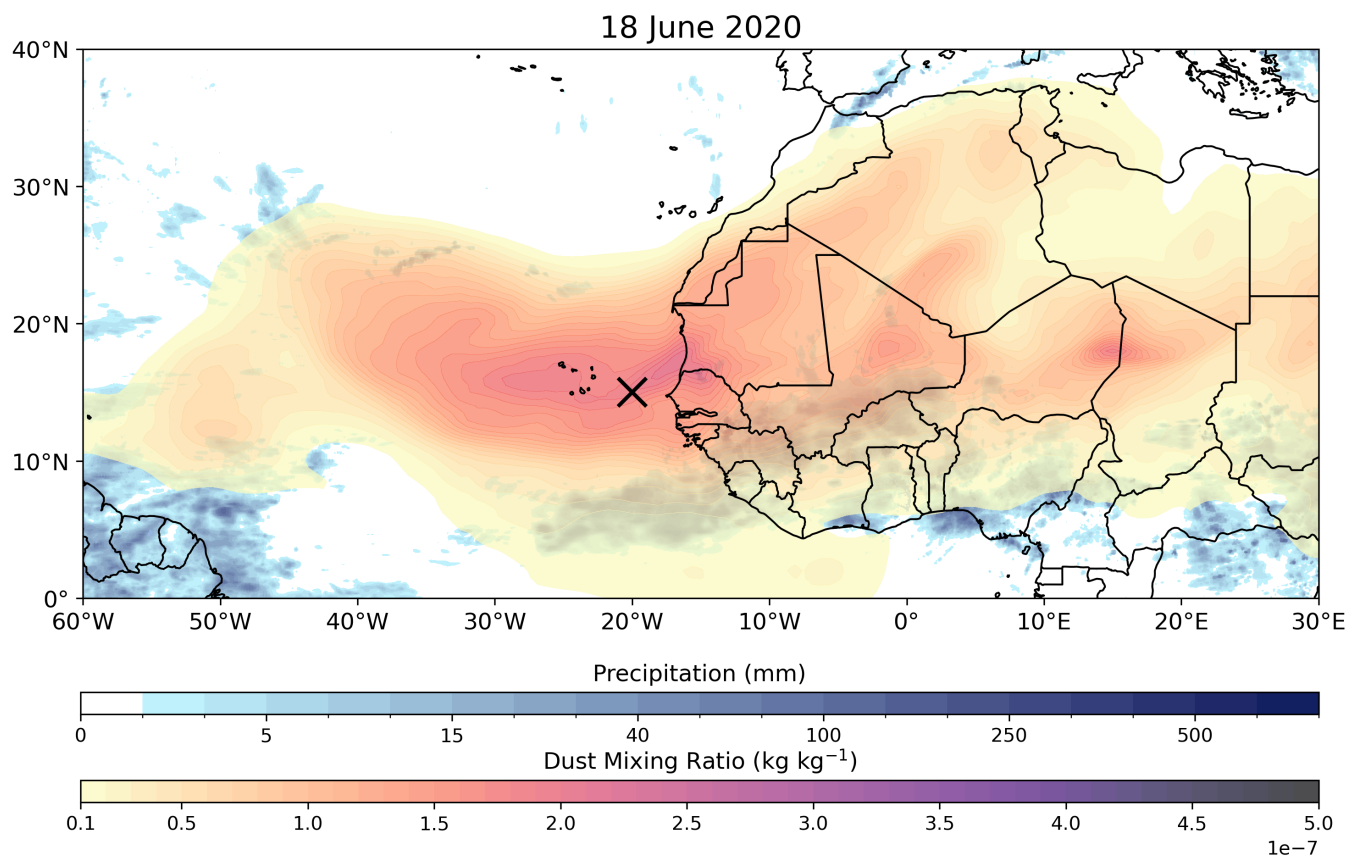
Figure 8. MERRA-2 total dust mixing ratio and IMERG daily accumulated precipitation on 18 June 2020. The location of the profile used in the analysis is marked in black.

rate is once again overestimated by both the MERRA-2 reanalysis below 800 hPa, with a heating rate of around 2.3 K/day at the surface for MERRA-2 and a heating rate. The SW heating rate at the surface from CAMS is similar to the heating rate from CPEX-CV, but the same increase in SW heating for CAMS between 950 hPa and 900 hPa reaches nearly 4.5 K/day. Above 800 hPa, the two reanalyses greatly underestimate the SW heating rate in this case, with differences of over 1 K/day between CPEX-CV and reanalysis. The CPEX-CV data reveals that the heating is evenly distributed throughout the column, whereas the reanalyses overestimate heating at the lower levels and underestimate heating at the upper levels. These differences in the structure of vertical heating will likely impact the forecast of the development of AEWs.

3.6 A note on clouds

It is crucial to emphasize that our investigation, utilizing CPEX-CV data and the Godzilla dust storm event, provides valuable insights into aerosol-induced heating variations. Radiation calculations primarily rely on dust fields and include parameters
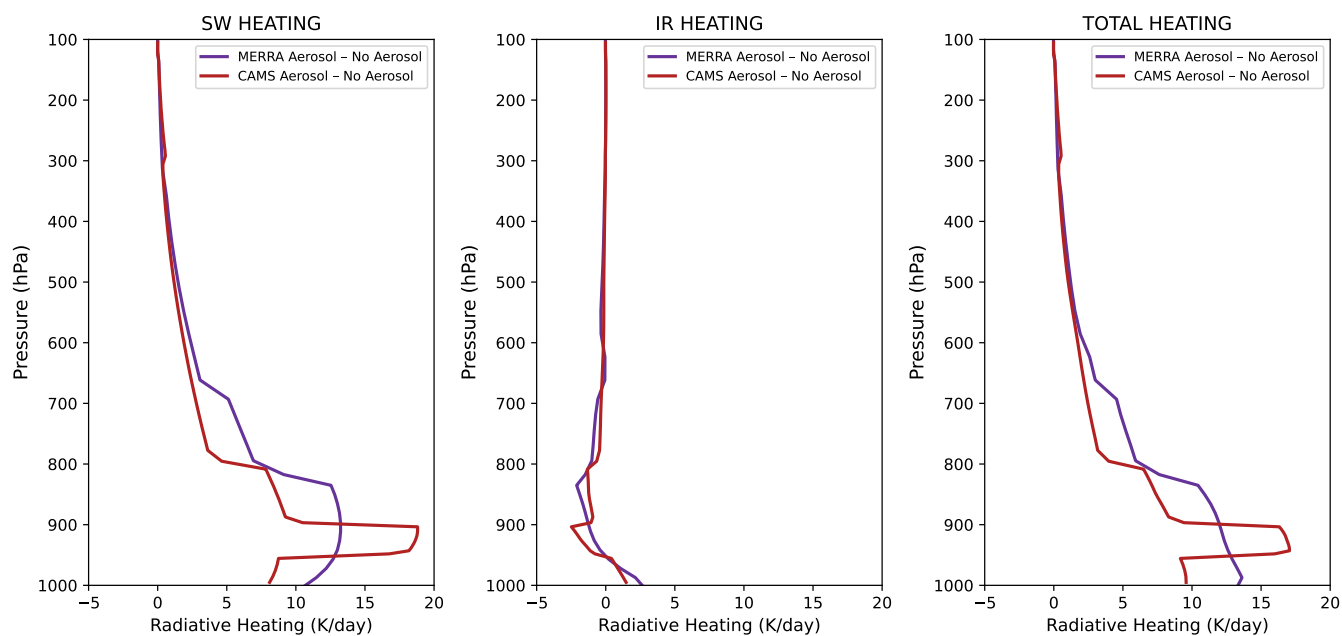
Figure 9. Heating rate difference between aerosol-aware and control run for MERRA-2 (purple) and CAMS (red) at 15°N, 20°W on 18 June 2020. The left panel shows SW heating, the center panel shows LW/IR heating and the right panel shows total heating.

such as pressure, temperature, moisture, and ozone profiles. The model acknowledges clouds based on moisture profiles but does not explicitly represent critical factors such as liquid water path and specific optical properties associated with clouds. This recognition highlights the limited scope of the cloud-related information provided by the model, underscoring the necessity for future research to integrate a more comprehensive treatment of cloud-related variables for a detailed understanding of atmospheric interactions.

4 Conclusions

The paper explores the intricate interactions between African Easterly Waves (AEWs) and Saharan dust using radiative examination techniques based on reanalysis and NASA airborne observations. The study leverages data from the Convective Processes Experiment – Cabo Verde (CPEX-CV) and multiple reanalysis datasets, including MERRA-2 and CAMS. The study examined seven DC-8 flights during the CPEX-CV field campaign, corresponding to 10 different AEWs, with a special emphasis on four waves that developed into named tropical storms, and two of them intensifying into hurricanes. The primary objectives include assessing the accuracy of reanalysis in depicting aerosol radiative properties, understanding the influence of aerosol heating rates, especially from Saharan dust, on AEW development, and evaluating the impact of aerosol assimilation
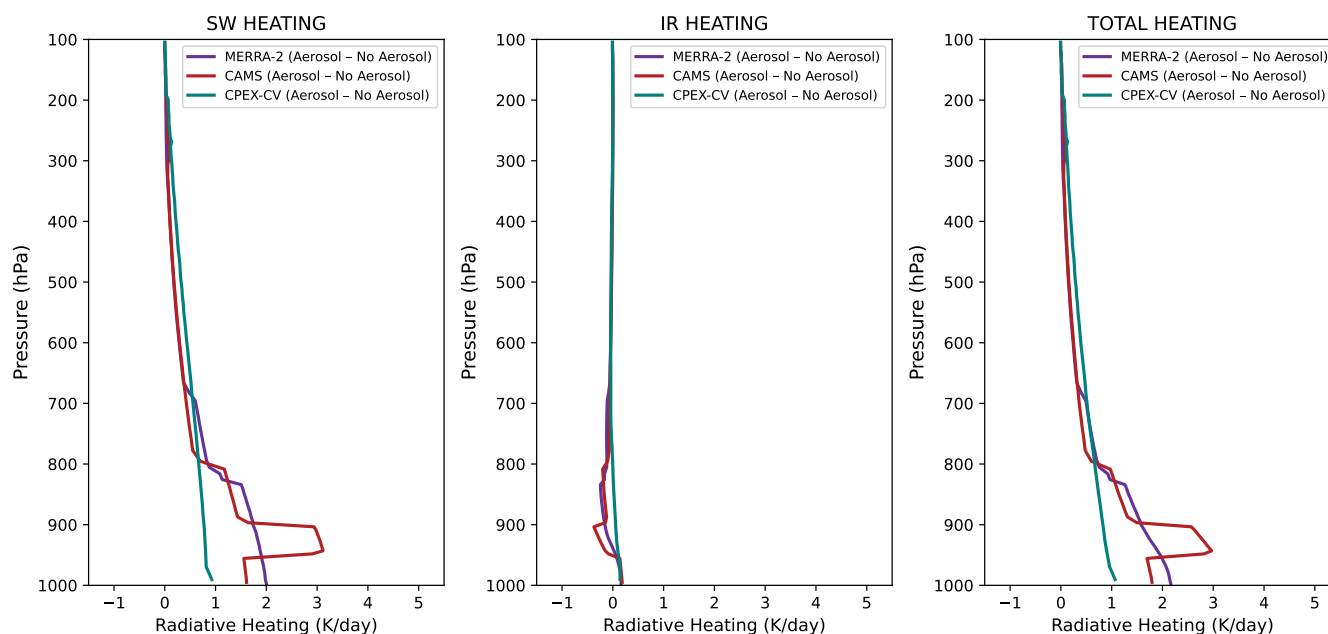
Figure 10. Heating rate difference between aerosol-aware and control run for MERRA-2 (purple), CAMS (red) and CPEX-CV (teal) on 09 September 2022. The left panel shows SW heating, the center panel shows LW/IR heating and the right panel shows total heating.

on model representation. The methodology integrates observational data from CPEX-CV with a four-stream radiative transfer
390 model (Fu-Liou-Gu RTM), utilizing aerosol profiles from MERRA-2 and CAMS reanalyses.

The research revealed significant variations in aerosol-induced heating rates between observed data and reanalyses, MERRA-
2 and CAMS as compared with heating rates calculated with the observational data collected over CPEX-CV. The reanalyses
exhibited significant differences compared to observed data, impacting the calculation of total heating rates. Both MERRA-2
and CAMS radiative transfer runs consistently overestimated shortwave (SW) heating rates below 800 hPa, even after assim-
395 ilating CPEX-CV data (which is the case for MERRA-2). This was due to notable disparities in the representation of aerosol
in extinction and aerosol optical depth (AOD). MERRA-2 exhibited higher surface extinction but missed variability through-
out the tropospheric column that was captured by observational data. On the other hand, CAMS consistently underestimated
aerosol extinction compared to the observational data, revealing challenges in accurately representing aerosol effects in models.
Both reanalyses also had too much AOD in background cases as contrasted with CPEX-CV data or too little in the anomalous
400 cases. A comparative analysis of an extreme dust event (June 2020 Godzilla dust storm) reinforced the findings, showcasing
differences in SW heating profiles between MERRA-2 and CAMS. This analysis provided further evidence of the robustness of
observed profiles and the model's ability to capture aerosol-induced heating variations. Finally, case studies focusing on Hur-
ricane Fiona and Tropical Storm Hermine illustrated the impact of aerosols on heating rates during specific research flights.
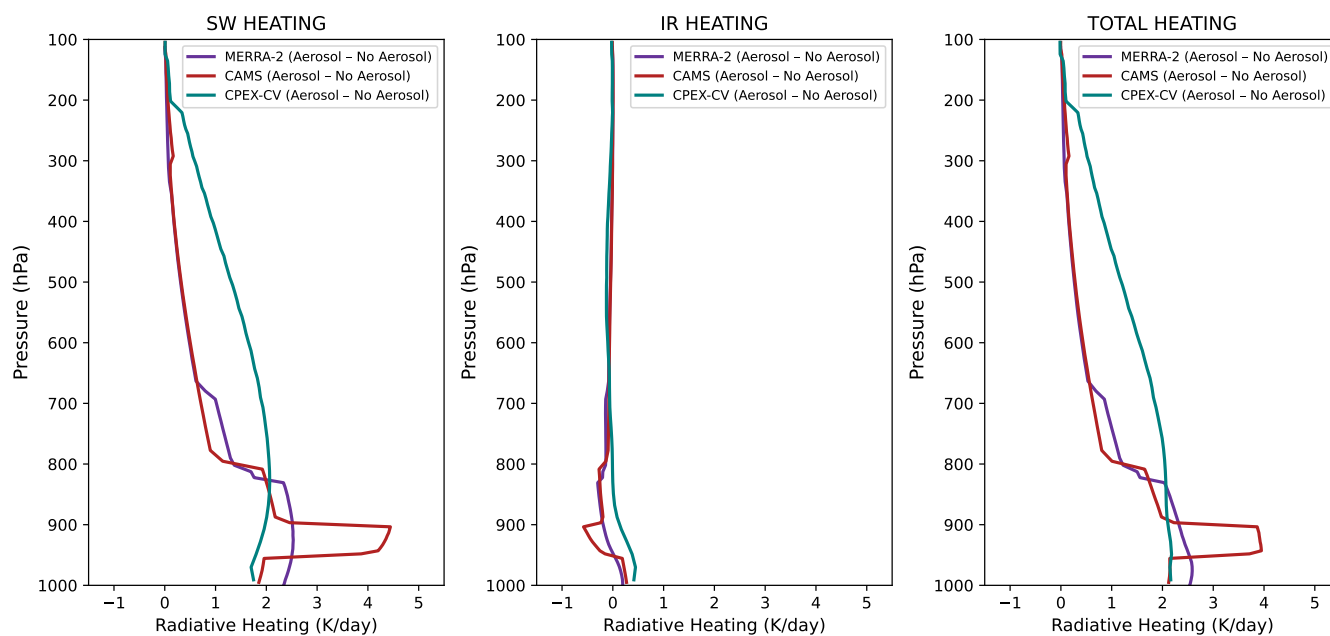
Figure 11. Heating rate difference between aerosol-aware and control run for MERRA-2 (purple), CAMS (red) and CPEX-CV (teal) on 22 September 2022. The left panel shows SW heating, the center panel shows LW/IR heating and the right panel shows total heating.

Both reanalyses exhibited notable discrepancies in SW heating rates compared to observed data, with potential implications
405　for forecasting the development of AEWs.

　　When considering the impact of heating rates on tropical cyclone development, a noteworthy observation emerges regarding the impact of varying dust concentrations on the process, particularly in relation to heating rates. The distinction between anomalous and background dust cases introduces a fascinating dynamic, unveiling a correlation between lower dust levels during the AEW development and the formation of exceptionally potent hurricanes (in the cases of Ian and Fiona). Strikingly,
410　when Hurricane Hermine was sampled, characterized by elevated dust concentrations, the storm exhibited a subsequent weakening and a short lived time span. Of course, it is essential to acknowledge that this analysis represents a gross simplification of a complex system, and a more comprehensive examination of environmental factors is imperative for a nuanced understanding. Despite this oversimplification, the observed patterns underscore the significance of incorporating dust-related variables in hurricane modeling studies. This warrants a more in-depth investigation to elucidate the intricate interplay between dust
415　concentrations, heating rates, and their influence on hurricane development, emphasizing the necessity for rigorous modeling studies to advance our comprehension of these intricate atmospheric phenomena.

　　The research significantly advances our understanding of the complex interactions between AEWs and Saharan dust, shedding light on the role of aerosol-induced heating rates in weather systems. The findings underscore the limitations of current reanalysis datasets in accurately capturing aerosol properties and their radiative effects, particularly in critical atmospheric

420 levels. Despite the assimilation of observational data, substantial differences persist, revealing the need for further refinement in modeling aerosol dynamics. The study emphasizes the importance of considering vertical distribution and composition of aerosols in assessing their impact on AEWs. The observed discrepancies in heating rates between reanalysis and observations at key atmospheric levels have implications for weather forecasting, emphasizing the need for improved aerosol parameterizations in NWP models. The comprehensive approach, combining airborne observations with advanced radiative transfer modeling,

425 provides valuable insights into the challenges and opportunities for refining our understanding of aerosol-climate interactions in the Atlantic basin.

Author contributions. RWB led the radiative transfer study. RWB and MIOM designed the experiments. RWB was responsible for obtaining datasets used as input for the radiative transfer calculations. RWB conducted the radiative transfer modeling and performed the majority of the analysis and was supervised and assisted by MIOM. RWB and MIOM prepared the manuscript and figures.

435 *Competing interests.* The authors declare that they have no conflict of interest.

References

Bauer, S. E. and Menon, S.: Aerosol direct, indirect, semidirect, and surface albedo effects from sector contributions based on the IPCC AR5 emissions for preindustrial and present-day conditions, Journal of Geophysical Research: Atmospheres, 117, 2012.

Bedka, K. M., Nehrir, A. R., Kavaya, M., Barton-Grimley, R., Beaubien, M., Carroll, B., Collins, J., Cooney, J., Emmitt, G. D., Greco, S., Kooi, S., Lee, T., Liu, Z., Rodier, S., and Skofronick-Jackson, G.: Airborne lidar observations of wind, water vapor, and aerosol profiles during the NASA Aeolus calibration and validation (Cal/Val) test flight campaign, Atmospheric Measurement Techniques, 14, 4305–4334, https://doi.org/10.5194/amt-14-4305-2021, 2021.

Buchard, V., Randles, C., Da Silva, A., Darmenov, A., Colarco, P., Govindaraju, R., Ferrare, R., Hair, J., Beyersdorf, A., Ziemba, L., et al.: The MERRA-2 aerosol reanalysis, 1980 onward. Part II: Evaluation and case studies, Journal of Climate, 30, 6851–6872, 2017.

Burpee, R. W.: The origin and structure of easterly waves in the lower troposphere of North Africa, Journal of the Atmospheric Sciences, 29, 77–90, 1972.

Carlson, T. N.: Some remarks on African disturbances and their progress over the tropical Atlantic, Monthly Weather Review, 97, 716–726, 1969.

Carlson, T. N. and Prospero, J. M.: The large-scale movement of Saharan air outbreaks over the northern equatorial Atlantic, Journal of Applied Meteorology and Climatology, 11, 283–297, 1972.

Dunion, J. P. and Velden, C. S.: The impact of the Saharan air layer on Atlantic tropical cyclone activity, Bulletin of the American Meteorological Society, 85, 353–366, 2004.

Fu, Q., Liou, K., Cribb, M., Charlock, T., and Grossman, A.: Multiple scattering parameterization in thermal infrared radiative transfer, Journal of the atmospheric sciences, 54, 2799–2812, 1997.

Gelaro, R., McCarty, W., Suárez, M. J., Todling, R., Molod, A., Takacs, L., Randles, C. A., Darmenov, A., Bosilovich, M. G., Reichle, R., et al.: The modern-era retrospective analysis for research and applications, version 2 (MERRA-2), Journal of climate, 30, 5419–5454, 2017.

GMAO: Supplemental Documentation for GEOS Aerosol Products, Tech. rep., NASA GMAO, 2023.

GOES-R Series Program: NOAA GOES-R Series Advanced Baseline Imager (ABI) Level 1b Data, NOAA National Centers for Environmental Information, https://doi.org/10.25921/tvws-w071, 2019.

Grogan, D. F. and Thorncroft, C. D.: The characteristics of African easterly waves coupled to Saharan mineral dust aerosols, Quarterly Journal of the Royal Meteorological Society, 145, 1130–1146, 2019.

Gu, Y., Liou, K., Ou, S., and Fovell, R.: Cirrus cloud simulations using WRF with improved radiation parameterization and increased vertical resolution, Journal of Geophysical Research: Atmospheres, 116, 2011.

Hess, M., Koepke, P., and Schult, I.: Optical properties of aerosols and clouds: The software package OPAC, Bulletin of the American meteorological society, 79, 831–844, 1998.

Hock, T. F., F. J. L.: The NCAR GPS Dropwindsonde, Bull. Amer. Meteor. Soc., 80, 407-420, 80, 407–420, 1999.

Huffman, G. J., Bolvin, D. T., Braithwaite, D., Hsu, K.-L., Joyce, R. J., Kidd, C., Nelkin, E. J., Sorooshian, S., Stocker, E. F., Tan, J., et al.: Integrated multi-satellite retrievals for the global precipitation measurement (GPM) mission (IMERG), Satellite Precipitation Measurement: Volume 1, pp. 343–353, 2020.

Inness, A., Ades, M., Agustí-Panareda, A., Barré, J., Benedictow, A., Blechschmidt, A.-M., Dominguez, J. J., Engelen, R., Eskes, H., Flemming, J., et al.: The CAMS reanalysis of atmospheric composition, Atmospheric Chemistry and Physics, 19, 3515–3556, 2019.

IPCC: Climate Change 2023: Synthesis Report. Contribution of Working Groups I, II and III to the Sixth Assessment Report of the Intergovernmental Panel on Climate Change [Core Writing Team, H. Lee and J. Romero (eds.)], IPCC, Geneva, Switzerland, 2023.

480 Jones, C., Mahowald, N., and Luo, C.: Observational evidence of African desert dust intensification of easterly waves, Geophysical research letters, 31, 2004.

Jury, M. R. and Santiago, M. J.: Composite analysis of dust impacts on African easterly waves in the Moderate Resolution Imaging Spectrometer era, Journal of Geophysical Research: Atmospheres, 115, 2010.

Karyampudi, V. M., Palm, S. P., Reagen, J. A., Fang, H., Grant, W. B., Hoff, R. M., Moulin, C., Pierce, H. F., Torres, O., Browell, E. V., et al.:
485 Validation of the Saharan dust plume conceptual model using lidar, Meteosat, and ECMWF data, Bulletin of the American Meteorological Society, 80, 1045–1076, 1999.

Landsea, C. W., Bell, G. D., Gray, W. M., and Goldenberg, S. B.: The extremely active 1995 Atlantic hurricane season: Environmental conditions and verification of seasonal forecasts, Monthly Weather Review, 126, 1174–1193, 1998.

Liou, K.-N., Fu, Q., and Ackerman, T. P.: A simple formulation of the delta-four-stream approximation for radiative transfer parameteriza-
490 tions, Journal of Atmospheric Sciences, 45, 1940–1948, 1988.

Lyapustin, A., Martonchik, J., Wang, Y., Laszlo, I., and Korkin, S.: Multiangle implementation of atmospheric correction (MAIAC): 1. Radiative transfer basis and look-up tables, Journal of Geophysical Research: Atmospheres, 116, 2011.

Ma, P.-L., Zhang, K., Shi, J. J., Matsui, T., and Arking, A.: Direct radiative effect of mineral dust on the development of African easterly waves in late summer, 2003–07, Journal of applied meteorology and climatology, 51, 2090–2104, 2012.

495 Mulcahy, J., Walters, D., Bellouin, N., and Milton, S.: Impacts of increasing the aerosol complexity in the Met Office global numerical weather prediction model, Atmospheric Chemistry and Physics, 14, 4749–4778, 2014.

Nalli, N. R. and Stowe, L. L.: Aerosol correction for remotely sensed sea surface temperatures from the National Oceanic and Atmospheric Administration advanced very high resolution radiometer, Journal of Geophysical Research: Oceans, 107, 36–1, 2002.

Nalli, N. R., Joseph, E., Morris, V. R., Barnet, C. D., Wolf, W. W., Wolfe, D., Minnett, P. J., Szczodrak, M., Izaguirre, M. A., Lumpkin,
500 R., et al.: Multiyear observations of the tropical Atlantic atmosphere: Multidisciplinary applications of the NOAA Aerosols and Ocean Science Expeditions, Bulletin of the American Meteorological Society, 92, 765–789, 2011.

Oyola, M. I.: Implementation of a Global Dust Physical Sea Surface Temperature Retrieval For Numerical Weather Prediction Applications, Ph.D. thesis, Howard University, 2015.

Oyola, M. I., Campbell, J. R., Xian, P., Bucholtz, A., Ferrare, R. A., Burton, S. P., Kalashnikova, O., Ruston, B. C., and Lolli, S.: Quantifying
505 the direct radiative effect of absorbing aerosols for numerical weather prediction: a case study, Atmospheric Chemistry and Physics, 19, 205–218, https://doi.org/10.5194/acp-19-205-2019, 2019.

Petty, G. W.: A First Course in Atmospheric Thermodynamics., Sundog Publishing, 2008.

Pratt, A. S. and Evans, J. L.: Potential impacts of the Saharan air layer on numerical model forecasts of North Atlantic tropical cyclogenesis, Weather and forecasting, 24, 420–435, 2009.

510 Ramanathan, V., Crutzen, P. J., Kiehl, J., and Rosenfeld, D.: Aerosols, climate, and the hydrological cycle, science, 294, 2119–2124, 2001.

Randles, C., Da Silva, A., Buchard, V., Colarco, P., Darmenov, A., Govindaraju, R., Smirnov, A., Holben, B., Ferrare, R., Hair, J., et al.: The MERRA-2 aerosol reanalysis, 1980 onward. Part I: System description and data assimilation evaluation, Journal of climate, 30, 6823–6850, 2017.

Reale, O., Lau, W. K., Kim, K.-M., and Brin, E.: Atlantic tropical cyclogenetic processes during SOP-3 NAMMA in the GEOS-5 global data
515 assimilation and forecast system, Journal of the atmospheric sciences, 66, 3563–3578, 2009.

Reale, O., Lau, K., and da Silva, A.: Impact of interactive aerosol on the African easterly jet in the NASA GEOS-5 global forecasting system, Weather and forecasting, 26, 504–519, 2011.

Reed, R., Klinker, E., and Hollingsworth, A.: The structure and characteristics of African easterly wave disturbances as determined from the ECMWF operational analysis/forecast system, Meteorology and Atmospheric Physics, 38, 22–33, 1988.

520 Reed, R. J., Norquist, D. C., and Recker, E. E.: The structure and properties of African wave disturbances as observed during phase III of GATE, Monthly Weather Review, 105, 317–333, 1977.

Thorncroft, C. and Blackburn, M.: Maintenance of the African easterly jet, Quarterly Journal of the Royal Meteorological Society, 125, 763–786, 1999.

Toll, V., Gleeson, E., Nielsen, K., Männik, A., Mašek, J., Rontu, L., and Post, P.: Impacts of the direct radiative effect of aerosols in numerical
525   weather prediction over Europe using the ALADIN-HIRLAM NWP system, Atmospheric Research, 172, 163–173, 2016.

Xu, F., Van Harten, G., Diner, D. J., Kalashnikova, O. V., Seidel, F. C., Bruegge, C. J., and Dubovik, O.: Coupled retrieval of aerosol properties and land surface reflection using the Airborne Multiangle SpectroPolarimetric Imager, Journal of Geophysical Research: Atmospheres, 122, 7004–7026, 2017.

Yu, H., Tan, Q., Zhou, L., Zhou, Y., Bian, H., Chin, M., Ryder, C. L., Levy, R. C., Pradhan, Y., Shi, Y., et al.: Observation and modeling of
530   the historic "Godzilla" African dust intrusion into the Caribbean Basin and the southern US in June 2020, Atmospheric Chemistry and Physics, 21, 12 359–12 383, 2021.

Zhang, J., Reid, J. S., Christensen, M., and Benedetti, A.: An evaluation of the impact of aerosol particles on weather forecasts from a biomass burning aerosol event over the Midwestern United States: observational-based analysis of surface temperature, Atmospheric Chemistry and Physics, 16, 6475–6494, 2016.